

# PROCEEDINGS OF SPIE

[SPIDigitalLibrary.org/conference-proceedings-of-spie](https://spiedigitallibrary.org/conference-proceedings-of-spie)

## Compact integrated photonic components for $\lambda=3-15$ micron

Swapnajit Chakravarty, Jason Midkiff, Kyoungmin Yoo, Chi-Jui Chung, Ali Rostamian, et al.

Swapnajit Chakravarty, Jason Midkiff, Kyoungmin Yoo, Chi-Jui Chung, Ali Rostamian, Ray T. Chen, "Compact integrated photonic components for  $\lambda=3-15$  micron," Proc. SPIE 10921, Integrated Optics: Devices, Materials, and Technologies XXIII, 109210D (4 March 2019); doi: 10.1117/12.2508885

**SPIE.**

Event: SPIE OPTO, 2019, San Francisco, California, United States

# Compact integrated photonic components for $\lambda=3-15$ micron

Swapnajit Chakravarty<sup>\*, a</sup>, Jason Midkiff, Kyoungmin Yoo, Chi-Jui Chung, Ali Rostamian, Ray T. Chen <sup>\*, a, b</sup>

<sup>a</sup>Omega Optics Inc., 8500 Shoal Creek Blvd., Bldg. 4, Suite 200,, Austin, TX, USA 78757

<sup>b</sup>Dept. of Electrical and Computer Engineering, University of Texas, 10100 Burnet Road Bldg. 160, Austin, TX, USA 78758;

## ABSTRACT

Chemicals are best recognized by their unique wavelength specific optical absorption signatures in the molecular fingerprint region from  $\lambda=3-15\mu\text{m}$ . In recent years, photonic devices on chips are increasingly being used for chemical and biological sensing. Silicon has been the material of choice of the photonics industry over the last decade due to its easy integration with silicon electronics as well as its optical transparency in the near-infrared telecom wavelengths. Silicon is optically transparent from  $1.1\mu\text{m}$  to  $8\mu\text{m}$  with research from several groups in the mid-IR. However, intrinsic material losses in silicon exceed  $2\text{dB/cm}$  after  $\lambda\sim 7\mu\text{m}$  ( $\sim 0.25\text{dB/cm}$  at  $\lambda=6\mu\text{m}$ ). In addition to the waveguiding core, an appropriate transparent cladding is also required. Available core-cladding choices such as Ge-GaAs, GaAs-AlGaAs, InGaAs-InP would need suspended membrane photonic crystal waveguide geometries. However, since the most efficient QCLs demonstrated are in the InP platform, the choice of InGaAs-InP eliminates need for wafer bonding versus other choices. The InGaAs-InP material platform can also potentially cover the entire molecular fingerprint region from  $\lambda=3-15\mu\text{m}$ . At long wavelengths, in monolithic architectures integrating lasers, detectors and passive sensor photonic components without wafer bonding, compact passive photonic integrated circuit (PIC) components are desirable to reduce expensive epi material loss in passive PIC etched areas. In this paper, we consider miniaturization of waveguide bends and polarization rotators. We experimentally demonstrate suspended membrane subwavelength waveguide bends with compact sub- $50\mu\text{m}$  bend radius and compact sub- $300\mu\text{m}$  long polarization rotators in the InGaAs/InP material system. Measurements are centered at  $\lambda=6.15\mu\text{m}$  for sensing ammonia.

**Keywords:** spectroscopy, photonic crystal waveguide, waveguides, infrared.

## 1. INTRODUCTION

Mid-infrared (Mid-IR) absorption spectroscopy based on integrated photonic circuits has shown great promise in trace-gas sensing [1] applications in which the mid-IR radiation directly interacts with the target analyte. This approach eliminates the needs of bulky gas cells and free-space optical components. Therefore, it has substantial advantages such as being lightweight, alignment-free, and offering high sensitivity sensing over conventional off-chip methods. [2,3] In addition, on-chip slow light enhanced slotted photonic crystal waveguides (PCWs) have demonstrated the ability to effectively increase light-matter interaction lengths and therefore higher detection sensitivity for the targeted gas analyte can be realized.[4,5] An ideal spectrometer needs to cover the entire molecular fingerprint region from  $\lambda=3-15\mu\text{m}$ .

Although silicon is the material of choice for most passive photonic applications, it is not suitable for wavelengths  $\lambda > 6\mu\text{m}$  due to its high intrinsic material loss. Germanium and GaAs are also suitable for covering the above wavelength range. However, in the design of photonic integrated spectrometers, we must also take into consideration that the light source in the mid-IR is primarily in the form of quantum cascade lasers (QCLs). The best performing room temperature mid-IR QCLs have been demonstrated till date in the InP material system. Three approaches exist for the integration of light sources and detectors with passive photonics. The first method includes a heterogeneous material integration of individual laser, detector and passive photonic waveguide. Heterogeneous integration requires precise free-space optical alignments and elaborate packaging, which introduces fragility and additional cost respectively for portable sensing applications in harsh environments. The second method involves bonding between III-V QCL epi and silicon via an appropriate interface with silicon dioxide or polymer that is typically characterized by high optical losses in almost the entire wavelength range mentioned above. The third method involves monolithic integration where the passive photonics

\*swapnajit.chakravarty@omegaoptics.com, [chenrt@austin.utexas.edu](mailto:chenrt@austin.utexas.edu);  
phone 1 512 996 8833; fax 1 512-471-8575;

Integrated Optics: Devices, Materials, and Technologies XXIII, edited by Sonia M. García-Blanco, Pavel Cheben,  
Proc. of SPIE Vol. 10921, 109210D · © 2019 SPIE · CCC code: 0277-786X/19/\$18 · doi: 10.1117/12.2508885

and the active quantum cascade laser/detector are fabricated on a bonding-free single epitaxially grown InP platform. The third method requires an epitaxial process to grow QCL/QCD layers along with the waveguide layers but essentially avoids till date high-cost and low-yield wafer/die bonding processes. At the same time, monolithic integration provides a low loss waveguiding platform with InGaAs core and InP cladding materials with material losses  $< 2$  dB/cm in the  $\lambda= 3$ - $15$   $\mu\text{m}$  wavelength range.

A photonic integration platform requires various passive photonic components such as waveguides [6], switches [7], and modulators [8] with active components such as lasers [9] detectors [10] and electronics [11] all of which have been experimentally demonstrated in the InP platform in the near-infrared (near-IR) but not necessarily for mid-IR range. In our final desired application of a monolithic spectrometer, a polarization rotator is needed on the input end to couple the transverse magnetic (TM) polarized emission from a QCL into previously demonstrated high sensitivity two-dimensional slotted PCWs that exhibit slow light effects and enhanced sensitivity for only the transverse electric (TE) polarization. The polarization rotator on the output end converts the polarization back to TM for detection by a monolithically integrated quantum cascade detector. Therefore, the polarization rotator is the essential component which helps integration with PCWs and thus enables high sensitivity trace gas sensing in a monolithic photonic integrated architecture. Various designs of near-IR polarization rotators have been reported in the literature [12] among which some of them require an extra masking/ alignment step such as in the dual-etched polarization rotator designs.

The passive photonic integration also requires compact waveguide bends that would allow dense packaging of sensors. The InGaAs/InP platform however has a low refractive index contrast between the core InGaAs and the cladding InP which necessitates a significantly large bend radius than the compact waveguide bends common in high index contrast silicon-on-insulator (SOI) platforms [13]. Recently, subwavelength waveguides have been experimentally demonstrated in the SOI platform for compact waveguides and bends by sacrificial etching of the lower cladding silicon dioxide.

In this paper, we experimentally demonstrate various designs for compact sub-wavelength waveguide bends and polarization rotators in the InP platforms, for common substrate integration with mid-infrared QCLs and QCDs. Our designs are centered at  $\lambda=6.15\mu\text{m}$  on the absorbance maximum of ammonia.

## 2. MID-INFRARED POLARIZATION ROTATOR

The schematic of a single-step etched PRS working at  $\lambda=6.15$   $\mu\text{m}$  in the InGaAs-InP platform is illustrated in Fig. 1(a). The waveguides are built on an InP ( $n=3.07$ ) substrate with a  $1.15$   $\mu\text{m}$  thick core layer of the InGaAs ( $n=3.36$ ), and a thin  $0.55$   $\mu\text{m}$  upper cladding of InP. The PRS operates around the waveguide width  $w=11$   $\mu\text{m}$  where the effective indices ( $N_{\text{eff}}$ ) of the  $\text{TM}_{00}$  and  $\text{TE}_{10}$  modes cross, as shown in Fig. 1(b-c). By adiabatically increasing the waveguide width around  $w=11$   $\mu\text{m}$ , the power in the input  $\text{TM}_{00}$  mode is effectively transferred into the  $\text{TE}_{10}$  mode due to the mode coupling.<sup>17</sup> Next, the  $\text{TE}_{10}$  mode is split by a Y-junction splitter into two single-mode  $\text{TE}_{00}$  modes with  $180$  degrees phase difference. A  $90$ -degree phase shift is introduced in the upper arm of the Y-splitter so that the  $\text{TE}_{00}$  modes are fed into the  $2\times 2$  multi-mode interferometer (MMI), with a total phase difference of  $90$  degrees. As a result, at the output end, as observed from three-dimensional (3D) finite difference time domain (FDTD) simulations, the majority of  $\text{TE}_{00}$  light will output from arm 1 as shown in Figs. 1(d-g). The PRS has three regions with increasing width taper which are optimized using Lumerical eigenmode expansion solver. In the final design, the pre-converter width increases from  $9.8$   $\mu\text{m}$  to  $10.7$   $\mu\text{m}$  over a length of  $1$  mm, whilst the post-converter width increases from  $11.3$   $\mu\text{m}$  to  $11.75$   $\mu\text{m}$  over  $0.1$  mm length. The primary section of the PRS is the middle converter section which in our design increases in width from  $10.7$   $\mu\text{m}$  to  $11.3$   $\mu\text{m}$ . The MMI is  $435$   $\mu\text{m}$  in length and  $22.7$   $\mu\text{m}$  in width. The phase shift is generated with waveguides of Bezier curves that give the required  $90$  degrees phase difference between the two arms.

For the characterization of the waveguide devices with end-fire coupling, it is necessary for the two output arms in Fig. 1(a) to be separated by at least  $1$  mm. The separation is achieved by S-bends that extend  $2$  mm and  $0.5$  mm along and perpendicular to the propagation direction. As observed in Fig. 1(i), nearly  $100\%$  conversion efficiency can be achieved for a pre-converter length of  $10$  mm and a corresponding converter length  $\sim 10$  mm. From the consideration of epitaxy cost in the preliminary proof-of-concept demonstration, we selected a converter length of  $2$  mm since the conversion efficiency deviation is relatively small, as observed in Fig. 1(h). The simulation in Fig. 1(h) indicates that  $47\%$  conversion efficiency from  $\text{TM}_{00}$  to  $\text{TE}_{00}$  can be expected over the total PRS length of  $3.04$  mm.

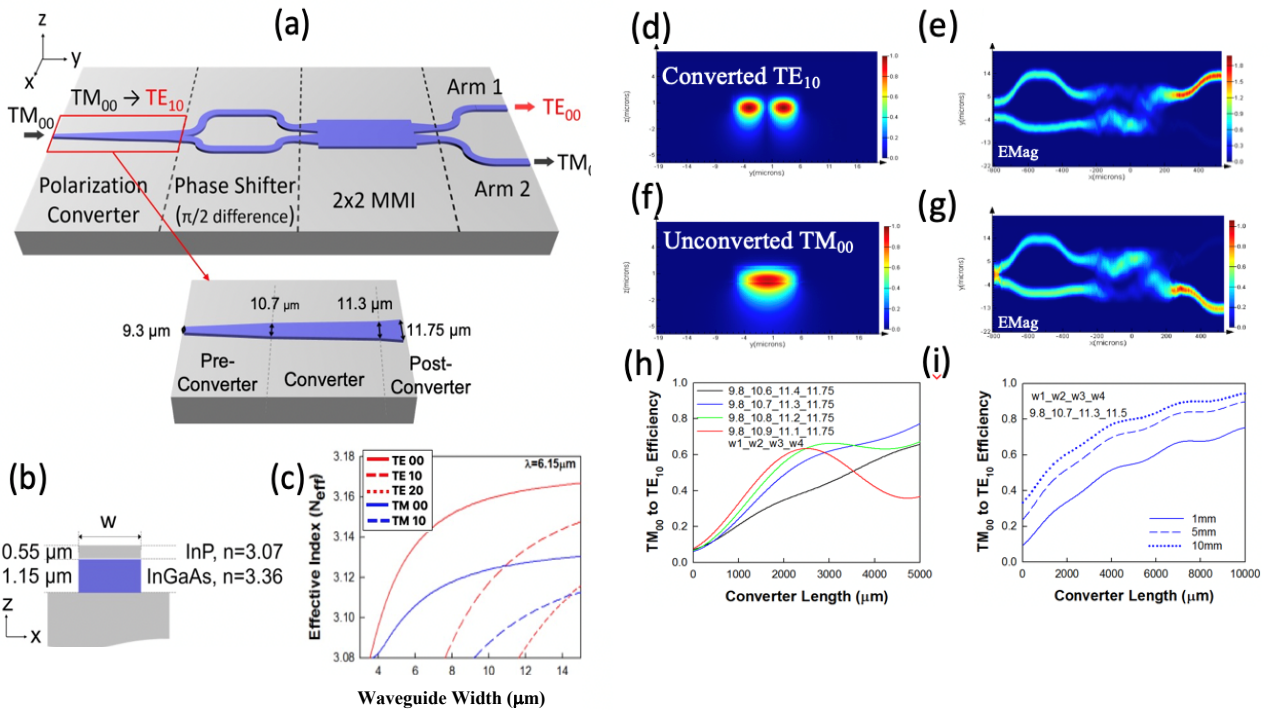


Figure 1: (a) Schematic diagram of the single-step etched polarization rotator-splitter (PRS) operating at  $6.15 \mu\text{m}$  in InGaAs-InP platform. Inset shows the details of the  $\text{TM}_{00}$  to  $\text{TE}_{10}$  conversion section, including pre-converter, converter and post-converter sections. (b) cross-section schematic and the epitaxy layer structures of the PRS, (c) the effective index versus InGaAs-InP waveguide width plot, (d)(e) modal distribution of converted  $\text{TE}_{10}$ , and (f)(g) modal distribution of unconverted  $\text{TM}_{00}$ . (h) Simulated conversion efficiency versus length of the converter section with converter width tolerance analysis.  $w_1$  to  $w_4$  are the widths at beginning of pre-converter, beginning of converter, beginning of post-converter and end of post converter respectively. (i) Converter efficiency with different lengths of the pre-converter.

Prior to the characterization of the PRS, first, the propagation loss of the mid-IR InGaAs/InP waveguides was characterized at  $\lambda=6.15 \mu\text{m}$ . 16 waveguides are defined with lengths varying lengths from 25.47 mm to 40.47 mm with 1 mm step by adding 500 $\mu\text{m}$  long sections on each vertical arm. The layout of the waveguides is as shown in the photomask patterns in Fig. 2(a). Each waveguide has 2 bends with radius  $R_1$  and another 2 bends in with radius  $R_2$ . The total length of each waveguide in the bent regions is constant. The waveguide width is selected as  $12 \mu\text{m}$ . The fabrication of the waveguides is done with photolithography and inductively coupled plasma (ICP) etching with plasma-enhanced chemical vapor deposition (PECVD) silicon oxide as the etching hard mask. A scanning electron microscope (SEM) image of a fabricated waveguide is shown in Fig. 2(b).

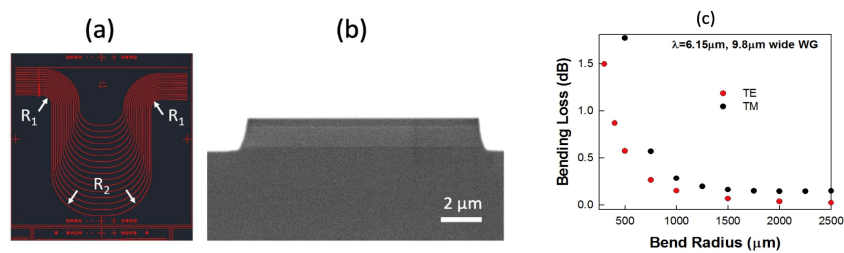


Figure 2: (a) Layout of waveguides for propagation loss measurements, with bending radii  $R_1$  and  $R_2$ . (b) SEM cross-section image of the fabricated InGaAs-InP waveguide in the PRS. (c) Bend loss related to modal mismatch at bent and straight interface in a 90-degree bend in a  $9.8 \mu\text{m}$  wide waveguide for the fundamental TE and TM modes at  $\lambda=6.15 \mu\text{m}$ .

After fabrication, the waveguides are then cleaved at the two edges and characterized with end-fire coupling setup. The laser light from a  $6.15 \mu\text{m}$  QCL is free-space coupled into the waveguides through a lens set. A wire grid polarizer (WGP) is placed between the lenses to confirm the polarization states. After routing from the waveguides, light is coupled into a mercury cadmium telluride (MCT) detector via a chalcogenide single mode fiber with a core size of 12

$\mu\text{m}$ . A lock-in amplifier, which is synchronized with the optical chopper, is connected to a MCT detector to read the output optical power. The fiber and the waveguides chip are placed on motorized 6-axis stages separately to achieve the best coupling condition. A half wave plate is inserted in the testing setup for to enable switching of the desired testing input light polarization of the input light. The output transmission of the waveguides with different lengths is measured and the loss versus the constant input power is plotted. Fig. 3(a) and Fig. 3(b) show the loss versus propagation length difference with input TM<sub>00</sub> and TE<sub>00</sub> polarized light respectively at  $\lambda=6.15 \mu\text{m}$ . It can be specially should be noted that the last three data points colored in red have a significantly higher loss than the rest of the waveguides. Those three data points correspond to the bottom three waveguides which have a sharp bending radius of 1400, 1200, and 1000  $\mu\text{m}$  (from top to bottom) in Fig. 2(a), and are excluded from the propagation loss analysis. The total propagation loss of the waveguide structures comprises the following three terms in Eq. 1.

$$\text{Total Loss} = [\#_{\text{interfaces}} \times 10 \log (P_{\text{bend}}/P_{\text{straight}})] + [\pi \times (R_1+R_2) \times \text{propagation loss}] + (L \times \text{propagation loss}) \quad (1)$$

The first term accounts for the modal mismatch at the interfaces between the bent region and straight region of the waveguides and is defined from the power coupling overlap between bent mode and straight mode. R<sub>1</sub> and R<sub>2</sub> denote respectively the bend radius of the two upper bends and two lower bends in each waveguide in Fig. 2(a). The second term and third term indicate the propagation losses in the bent and straight regions. As shown in Fig.2(c), when the bending radii are larger than 1500  $\mu\text{m}$  at 6.15  $\mu\text{m}$  wavelength, the additional propagation losses in the bent regions can be neglected. Therefore, they can be treated as typical straight waveguides and we can use the cut-back method to calculate the losses.

A linear fitting for propagation loss is done excluding the three data points. From the linear fit, the calculated mode propagation loss of the waveguide is obtained as 4.19 dB/cm for the TM mode and 3.25 dB/cm for the TE mode as shown in Fig. 3(c-d).

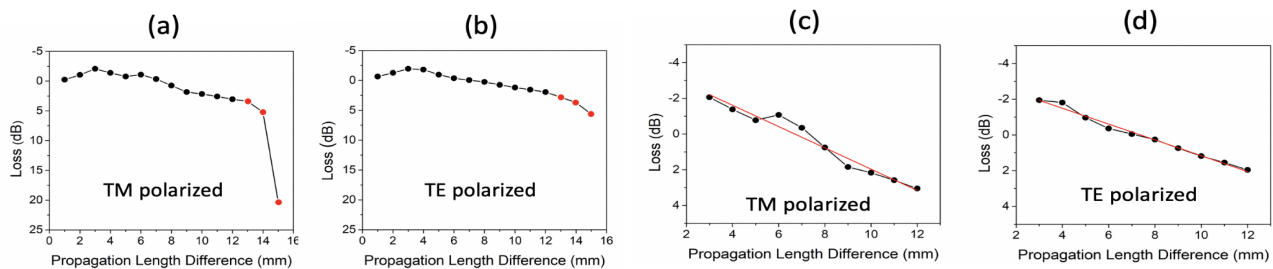


Figure 3: Loss versus propagation length difference plot for (a) TM polarized input, and (b) TE polarized input. Loss data and linear fitting, excluding waveguides red data points in (a) and (b) for (c) TM polarized input, and (d) TE polarized input.

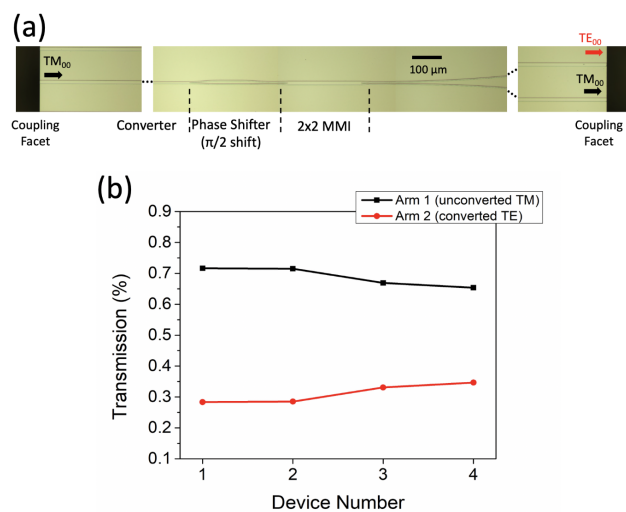


Figure 4: (a) Stitched optical microscope images of the fabricated PRS, and (b) Transmission of the two output arms for four devices with identical parameters.

Fig. 4 shows the stitched optical microscope image of the fabricated PRS device and the measured results. Four devices with identical geometrical parameters are fabricated and tested. The input optical power focused to the input facet is 1.38 mW. The averaged unconverted TM output light is 58.52  $\mu$ W and the averaged converted TE output light is 26.51  $\mu$ W. From strip waveguide measurements, considering the waveguide propagation loss is 4.19 dB/cm for TM and 3.25 dB/cm for TE, the averaged coupling loss of two as-cleaved facets is calculated to be 2.7 dB for TM<sub>00</sub> mode and 2.78 dB for TE<sub>00</sub> mode. Therefore, we can estimate the insertion loss of our proposed 3.04 mm long PRS as 4.67 dB which includes ~0.2 dB loss at the MMI [14] and ~1 dB loss at the Y-junction splitter [15] as typically obtained in near-IR measurements. The four PRSs demonstrate an averaged conversion efficiency of 31.2% at the upper arms.

A single-step etched polarization rotator-splitter, operating at 6.15  $\mu$ m wavelength in the InGaAs-InP material system is designed, fabricated and characterized. Simulations indicate that a near 100% conversion efficiency can be achieved by the adiabatic transfer of power from the fundamental TM<sub>00</sub> to TE<sub>10</sub> mode, prior to conversion to TE<sub>00</sub> with a 10 mm long converter section and a 10mm long pre-converter section. Our proof-of-concept device with 2 mm long converter section, and 1mm long pre-converter section demonstrates experimentally 31.2 % conversion efficiency versus 47 % obtained in simulations. The difference in experimental versus simulated conversion efficiency in our PRS can be attributed to fabrication imperfections, such as deviations in widths of the various PRS sections, as well as modal losses at the cleaved facets.

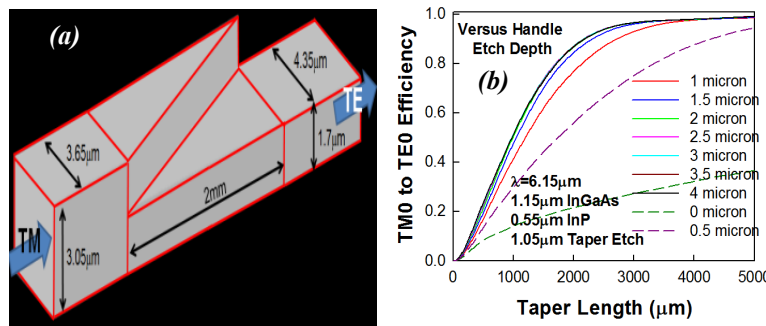


Figure 5: (a) Schematic of a 2mm long dual etch polarization rotator (b) Simulated direct TM<sub>00</sub> to TE<sub>00</sub> conversion efficiency.

Although the single etch polarization rotator demonstrated here offers ease of fabrication, a device with 100% conversion would occupy significant area on the chip which translates to higher cost. Simulations indicate that a device that achieves 100% conversion efficiency would need the polarization converter section from TM<sub>00</sub> to TE<sub>10</sub> to be 20mm long. We designed a dual etched tapered waveguide polarization rotator converting TM<sub>00</sub> directly to TE<sub>00</sub>, shown in Fig. 5(a), which achieved >90% polarization rotation over a ~2mm length at  $\lambda=6.15\mu\text{m}$  as shown in Fig. 5(b) [16].

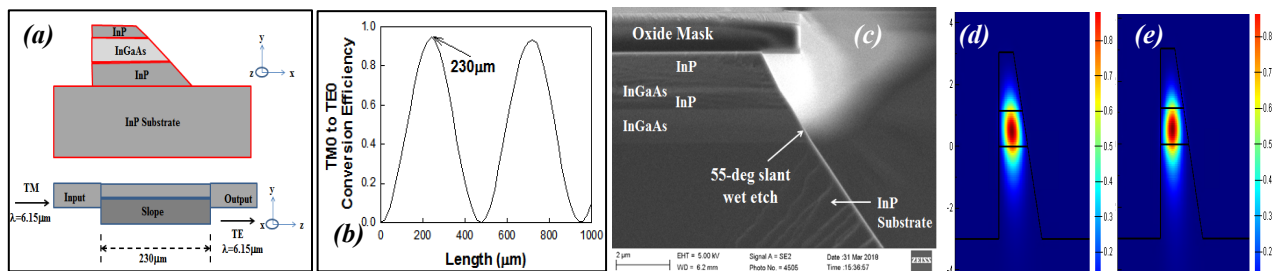


Figure 6: (a) Schematic of compact polarization rotator at  $\lambda=6.15\mu\text{m}$ . (b) Conversion efficiency versus length showing beating pattern of maximum and minimum conversion (c) 55-degree wet etched angle in Br-CH<sub>3</sub>OH etch along <111> plane in epi layers of InGaAs and InP on InP substrate, showing fabrication feasibility. Tilted intermediary modes (d) and (e) beat in compact TM<sub>0</sub> to TE<sub>0</sub> conversion.

Fig. 6(a) schematically shows the cross-section of a third polarization rotator design at  $\lambda=6.15\mu\text{m}$  that achieves ~95% conversion efficiency over only 230 $\mu\text{m}$  length (Fig. 6(b)). [17] It employs the preferential <111> wet etching of InGaAs/InP materials to form a trapezoid with one 55-degree sidewall facet (Fig. 6(c)) that results in two modes tilted with respect to the fundamental TM<sub>0</sub> input and TE<sub>0</sub> output modes (Fig. 6(d) and 6(e)). The length of the polarization rotator is determined by the beat length of the tilted modes. The polarization conversion efficiency is practically constant for etch depths >2 $\mu\text{m}$  into the handle InP. The 1dB bandwidth of the specific design here extends from  $\lambda=5.4\mu\text{m}$ -6.3 $\mu\text{m}$ .

The 1dB width tolerance at the top of the upper cladding InP is  $\Delta w \sim 500\text{nm}$ . The 1 dB length tolerance of the polarization rotation section is  $\sim \pm 50\mu\text{m}$ . The fabrication procedure has been verified (Fig. 6(c)). Experimental results will be presented in the future.

### 3. SUBWAVELENGTH WAVEGUIDE BENDS

Simulations in Fig. 7(a) indicate that the minimum waveguide bend radius, for a fixed core thickness in Fig. 1(b), is dependent on the top cladding thickness. The top cladding thickness determines the spacing between the eventual QCL active region and the underlying InGaAs waveguide. A thicker cladding increases the coupling taper length. The minimum 90-degree bend loss saturates to  $\sim 0.35\text{dB/bend}$  for cladding thicknesses greater than  $1.5\mu\text{m}$ , with a minimum bend radius  $\sim 500\mu\text{m}$ . The bending loss calculation takes into consideration the experimentally measured waveguide propagation loss. At a cladding thickness  $1\mu\text{m}$ , the minimum bend loss is  $\sim 0.5\text{dB}$  at a bend radius  $\sim 750\mu\text{m}$ . However, if the cladding thickness is reduced to  $0.55\mu\text{m}$ , the required bend radius is  $\sim 3.25\text{mm}$ , with 90-degree bend loss  $\sim 2.1\text{dB}$ . Experimental measurements in Fig. 7(c) indicate that propagation loss increases significantly for strip waveguides with bend radius  $< 1\text{mm}$ . For beam steering applications where several waveguides need to be spaced at  $\lambda/2$  periodicity ideally, (typically  $> 2\lambda$  experimentally), at  $\lambda = 6.15\mu\text{m}$ , waveguides need to be routed with S-bends and spaced  $\sim 12\mu\text{m}$  apart. In monolithic on-chip sensing, with integrated arrays of QCLs and QCDs, efficient utilization of area on chip requires a separation between individual DFBs by  $\sim 200\mu\text{m}$  by considering conservatively, a wire bonding pad of width  $\sim 100\mu\text{m}$ . Such a layout would be facilitated by sharper bends than that feasible with a simple core-cladding architecture in Fig. 1(b). We mention here that for waveguides with ridge widths  $\sim 9\text{--}10\mu\text{m}$ , similar to ridge widths of QCLs at  $\lambda \sim 6.15\mu\text{m}$ , the bending loss of the fundamental TM mode reaches a minimum  $\sim 0.9\text{dB}$  for  $1\text{mm}$  bend radius, irrespective of cladding height from  $0.55\mu\text{m}$  to  $2\mu\text{m}$ .

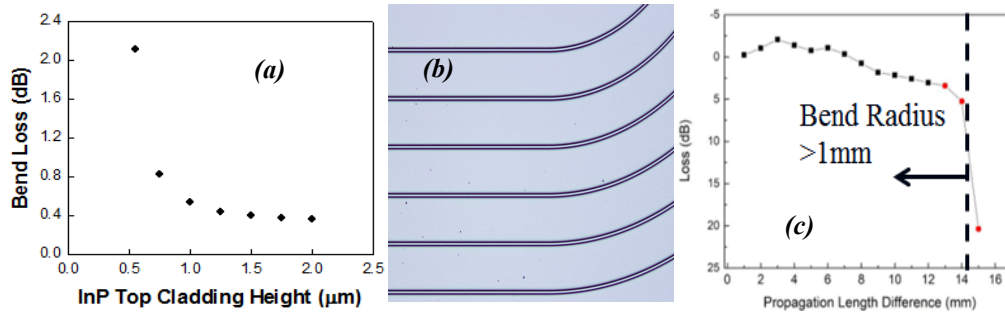


Figure 7: (a) Bend loss of the waveguide in (a) with  $w=5\mu\text{m}$ , versus top InP cladding height. (b) Microscope image of curved waveguide sections with large bend radii. (c) Experimental measurements confirming increased bend loss at bend radius  $< 1\text{mm}$

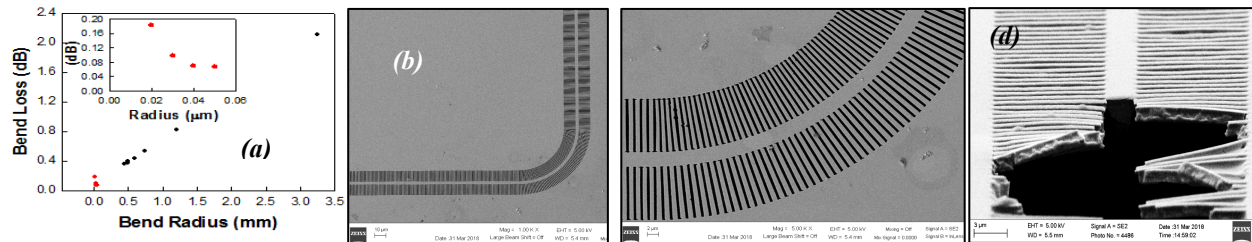


Figure 8: Bend loss as a function of bend radius for (black dots)  $5.875\mu\text{m}$  wide InGaAs waveguide with  $1.9\mu\text{m}$  top cladding and (red dots) subwavelength waveguide of width  $w=3\mu\text{m}$ . (Inset) shows magnified image of bend loss versus bend radius for SWW with  $50\mu\text{m}$  bend radius with SEM in (b). (c) Top view and (d) cross section SEM of suspended membrane SWW in InGaAs/InP. (c) Top view indicates robustness of suspended membrane. Broken fins in (d) are a result of cleaving to view cross-section

In recent years, subwavelength waveguides (SWWs), or subwavelength metamaterial clad waveguides, defined by a periodic array of etched holes bordering a strip waveguide, have been proposed as effective means to circumvent the cladding limitations, when appropriate high index core materials are available. The etched holes allow easy access of the wet etchant for sacrificial etch based removal of the underlying cladding. Diffraction effects are suppressed by choosing

a lattice periodicity that is less than half the Bragg period. The undercut strip waveguide, clad by air on top and bottom, is  $3\mu\text{m}$  wide, supported by 10 micron wide metamaterial fins. Simulations indicate that 90-degree bend radii less than  $50\mu\text{m}$  can be easily achieved with similar bend losses as in non-suspended structures in Fig. 8(a). The subwavelength period is chosen as  $1\mu\text{m}$  for TE and  $1.15\mu\text{m}$  for TM polarization. Figs. 8(b-d) show SEM images of the fabricated subwavelength metamaterial waveguide bends. Figs. 8(c) and (d) show top view and cross-sectional view of a typical suspended membrane subwavelength waveguide in InGaAs/InP. Top and cross-section SEMs indicate robustness of suspended InGaAs structures and viability as tight confinement and slow light waveguides in  $\lambda=3\text{-}15\mu\text{m}$  range. The measured transmitted TM output for a 2mm long suspended membrane  $3\mu\text{m}$  wide InGaAs waveguide with  $10\mu\text{m}$  fins, and 5mm long input and output un-suspended waveguides was  $\sim 12.5\mu\text{W}$ , compared to  $\sim 15\mu\text{W}$  for a 12mm long un-suspended InGaAs/InP waveguide for the same input power and input and output facets. More measurements are needed, but it was validated that high transmission is observed. Elsewhere 0.82dB/cm propagation losses have been observed in suspended membrane silicon waveguides [13].

#### 4. SUMMARY

In summary, we experimentally demonstrated mid-infrared polarization rotator and suspended membrane subwavelength waveguides and waveguide bends on the InGaAs/InP platform for operation at  $\lambda=6.15\mu\text{m}$ . The InGaAs/InP passive waveguiding material system was chosen to enable a common substrate architecture integrating QCLs and QCDs in the InP material system. Compact sub- $50\mu\text{m}$  waveguide bends were experimentally demonstrated. Designs were presented for compact  $230\mu\text{m}$  long polarization rotator that will be demonstrated in future research.

#### ACKNOWLEDGEMENTS

The research was funded by the Army (ARO) STTR Contract #W911NF-17-P-0056. The authors also acknowledge the use of Texas Nanofabrication Facilities supported by the NSF NNCI Award #1542159.

#### REFERENCES

- [1] Y.. Zou, S. Chakravarty, C.-J. Chung, X. Xu, and R. T. Chen, "Mid-infrared silicon photonic waveguides and devices [Invited]," *Photonics Research*, 6, 254 (2018).
- [2] A. Gurlo and R. Riedel, "In situ and operando spectroscopy for assessing mechanisms of gas sensing," *Angewandte Chemie International Edition*, 46, 3826 (2007).
- [3] M. Lackner, "Tunable diode laser absorption spectroscopy (TDLAS) in the process industries—a review," *Reviews in Chemical Engineering*, 23, 65 (2007).
- [4] W.-C. Lai, S. Chakravarty, Y. Zou, and R. T. Chen, "Multiplexed detection of xylene and trichloroethylene in water by photonic crystal absorption spectroscopy," *Optics Letters*, 38, 3799 (2013).
- [5] Y. Zou, S. Chakravarty, P. Wray, and R. T. Chen, "Mid-infrared holey and slotted photonic crystal waveguides in silicon-on-sapphire for chemical warfare simulant detection," *Sensors and Actuators B: Chemical*, 221, 1094 (2015).
- [6] X. Letartre, C. Seassal, C. Grillet, P. Rojo-Romeo, P. Viktorovitch, M. Le Vassor d'Yerville, D. Cassagne, and C. Jouanin, "Group velocity and propagation losses measurement in a single-line photonic-crystal waveguide on InP membranes," *Applied physics letters*, 79, 2312 (2001).
- [7] T. Tanemura, I. M. Soganci, T. Oyama, T. Ohyama, S. Mino, K. A. Williams, N Calabretta, H. J. S. Dorren, and Y. Nakano , "Large-capacity compact optical buffer based on InP integrated phased-array switch and coiled fiber delay lines," *Journal of Lightwave Technology*, 29, 396 (2011).

- [8] Y. Ogiso, J. Ozaki, Y. Ueda, N. Kashio, N. Kikuchi, E. Yamada, H. Tanobe, S. Kanazawa, H. Yamazaki, Y. Ohiso, T. Fujii, and M. Kohtoku, "Over 67 GHz Bandwidth and 1.5 V  $V\pi$  InP-Based Optical IQ Modulator With nipi Heterostructure," *Journal of Lightwave Technology*, 35, 1450 (2017).
- [9] S. Lange, S. Wolf, J. Lutz, L. Altenhain, R. Schmid, R. Kaiser, M. Schell, C. Koos, and S. Randel, "100 GBd Intensity Modulation and Direct Detection With an InP-Based Monolithic DFB Laser Mach-Zehnder Modulator," *Journal of Lightwave Technology*, 36, 97 (2018).
- [10] C. Yu, M. Shangguan, H. Xia, J. Zhang, X. Dou, and J.-W. Pan, "Fully integrated free-running InGaAs/InP single-photon detector for accurate lidar applications," *Optics Express*, 25, 14611 (2017).
- [11] M. Urteaga, Z. Griffith, M. Seo, J. Hacker, and M. J. Rodwell, "InP HBT technologies for THz integrated circuits," *Proceedings of the IEEE*, 105, 1051 (2017).
- [12] Y. Ding, H. Ou, and C. Peucheret, "Wideband polarization splitter and rotator with large fabrication tolerance and simple fabrication process," *Optics Letters*, 38, 1227 (2013).
- [13] J. Soler Penades, A. Ortega-Moñux, M. Nedeljkovic, J. G. Wangüemert-Pérez, R. Halir, A. Z. Khokhar, C. Alonso-Ramos, Z. Qu, I. Molina-Fernández, P. Cheben, and G. Z. Mashanovich, "Suspended silicon mid-infrared waveguide devices with subwavelength grating metamaterial cladding" *Opt. Exp.* 24(20), 22908 (2016)
- [14] A. Hosseini, D. N. Kwong, Y. Zhang, H. Subbaraman, X. Xu, and R. T. Chen, "1 × N Multimode Interference Beam Splitter Design Techniques for On-Chip Optical Interconnections," *IEEE J. Sel. Top. Quantum Electron.* 17(3), 510 (2011).
- [15] G. T. Reed, *Silicon Photonics: The State of the Art*, Wiley, 2008.
- [16] J. Zhang, T.-Y. Liow, M. Yu, G.-Q. Lo, and D.-L. Kwong, "Silicon waveguide based TE mode converter," *Optics Express*, 18, 25264 (2010).
- [17] S. Adachi and H. Kawaguchi, "Chemical etching characteristics of (001) InP," *Journal of The Electrochemical Society*, 128, 1342 (1981).